RSC Advances

PAPER

View Article Online
View Journal | View Issue

Cite this: *RSC Adv.*, 2023, **13**, 34291

Self-assembled boron nitride nanosheet-based aerogels as support frameworks for efficient thermal energy storage phase change materials†

Lanshu Xu, [a] Yujie Ding[a] and Laishun Wang*[b]

Received 9th August 2023
Accepted 16th November 2023

DOI: 10.1039/d3ra05389j

rsc.li/rsc-advances

Phase change materials (PCMs) are promising in many fields related to energy utilization and thermal management. However, the low thermal conductivity and poor shape stability of PCMs restrict their direct thermal energy conversion and storage. The desired properties for PCMs are not only high thermal conductivity and excellent shape stability, but also high latent heat retention. In this study, the boron nitride nanosheets (BNNSs) were bridged by small amounts of GO nanosheets and successfully self-assembled into BNNS/rGO (BG) aerogels by hydrothermal and freeze-drying processes. The BG aerogels with interlaced macro-/micro-pores have been proven to be ideally suited as support frameworks for encapsulating polyethylene glycol (PEG). The obtained composite PCMs exhibit high thermal conductivity (up to 1.12 W m^{-1} K^{-1}), excellent shape stability (maintain at 90 °C for 10 min), and high latent heat (187.2 J g^{-1}) with a retention of 97.3% of the pure PEG, presenting great potential applications in energy storage systems and thermal management of electronic devices.

1. Introduction

Boron nitride nanosheets (BNNSs), also called "white graphene", have drawn broad and increasing attention due to the unique physical properties.[1,2] Specifically, BNNSs have excellent intrinsic in-plane thermal conductivity (1700–2000 W m^{-1} K^{-1}), low dielectric constant (3–4), high chemical/thermal stability, extraordinary mechanical and electrical insulation properties.[3,4] Hence, these superior properties enable the potential applications of BNNSs in thermal management materials,[5,6] electrocatalysts,[7] high-temperature coating,[8] and sorbents.[9] However, it is difficult to fabricate BNNS-based composites due to the lack of surface functional groups in BNNSs, especially for the assembly of three-dimensional (3D) BNNS aerogels. Currently, the fabrication of 3D BNNS aerogels is tactfully achieved by utilizing template methods to accommodate BNNSs.[10–12] For example, Xue *et al.* used melamine foam (MF) as a template to incorporate reduced graphene oxide (rGO)/BNNSs to form composite MF/rGO/BN aerogel, exhibiting a high thermal conductivity of 0.79 W m^{-1} K^{-1} after impregnation with polyethylene glycol (PEG).[13] In addition to this there are 3D printing method,[14] and low-dimensional BN assembly method.[15] However, with the rise of green chemistry, researchers are committed to using self-assembly method without the generation of other by-products, and focus on developing more efficient and economical strategies for the synthesis and functionalization of BNNS aerogels.

3D BNNS aerogels with high thermal conductivity and porous structure are highly anticipated to be carriers of phase change materials (PCMs).[16] Polyethylene glycol (PEG), as a typical "solid–liquid" PCM is widely used in waste heat recovery due to the advantages of suitable phase change temperature and high energy storage density.[17,18] However, PEG faces problems such as leakage and slow heat absorption/exhaustion rate in practical applications. Based on the stable 3D thermally conductive BNNS networks, the PCMs can keep shape stability and effectively avoid the leakage during the liquidation and solidification cycles.[19] Meanwhile, strongly linked BNNSs form efficient filler–filler overlaps, which can increase the high thermal conductivity and thus achieve high heat transfer efficiency.[20] For example, Wan *et al.* prepared L-glutamine-grafted BNNSs/nanofibers/PEG-based PCM with a high latent heat of 150.1 J g^{-1}.[11] Xue *et al.* obtained MF/rGO/BN/PEG-based PCM with a high latent heat of 160.7 J g^{-1} and a retention of 90.8% of pure PEG.[13] Thus, facile strategy to assemble PCMs by using more effective 3D BNNS networks without sacrificing their latent heat is still an urgent target to pursue.[21]

In this work, we proposed an effective strategy to assemble 3D BNNS-based aerogels by using small amount of GO nanosheets. The GO nanosheets act as initiators for the self-assembly of BNNSs due to their good water solubility and self-assembly properties during the reduction process.[22,23] Based on affinity interactions between GO and BNNS, the BNNSs bridged by GO

[a]*Zhuhai Fudan Innovation Institution, Zhuhai, 518057, China*
[b]*Sino-French Institute for Nuclear Energy and Technology, Sun Yat-sen University, Zhuhai, 519080, China. E-mail: wanglaish@mail.sysu.edu.cn*

† Electronic supplementary information (ESI) available. See DOI: https://doi.org/10.1039/d3ra05389j

nanosheets can form continuous thermal conductivity paths, and successfully self-assembled into aerogels with interlaced macro-/micro-pores. After impregnation of PEG, it is interesting to observe that the prepared composite PCMs show enhanced thermal conductivity, excellent shape stability, high latent heat of fusion and latent heat retention.

2. Experimental

2.1 Materials

Hexagonal boron nitride (h-BN, PT110) powders were purchased from Momentive Performance Materials. Graphene oxide (GO) was purchased from Hangzhou Gaoxi Technology Co., Ltd. Isopropyl alcohol (IPA, ≥99.5%) was provided by Aladdin Biochemical Technology Co., Ltd. Deionized (DI) water was obtained in the laboratory using Millipore Elix (Elix Technology inside, USA). Polyethylene glycol (PEG, $M_n = 10\,000$) was purchased from Shanghai Bide Pharmaceutical Technology Co., Ltd.

2.2 Methods

2.2.1 Preparation of BNNSs. The exfoliation of h-BN was prepared *via* ball milling method using IPA as a liquid phase assistant. Typically, pristine h-BN (5 g), IPA (20 mL), and two different size ZrO_2 balls with diameters of 10 mm (100 g) and 2 mm (25 g) were loaded into a ZrO_2 tank (a volume of 250 mL). The tank was rotated at a speed of 300 rpm in a planetary ball mill (XH-QMQX, Chang Sha MITR, China) for 12 h. The milled paste was dispersed in DI water and centrifuged at 1000 rpm (TGL-15B, Shanghai Anting Scientific Instrument, China) for 30 min for further purification. Then the purified samples were centrifuged at 10 000 rpm for 30 min to remove the supernatant. Finally, the BNNS slurry was freeze-dried to powder for subsequent use.

2.2.2 Preparation of BNNS/rGO (BG) aerogels. The BG aerogel was prepared by hydrothermal self-assembly and freeze-drying processes. As shown in Fig. 1a, a certain amount of BNNSs (1.52 g) was added into the GO solution (2.0 mg mL^{-1}, 40 mL) in a conical flask, followed by magnetic stirring (500 W, 2 h) for thorough mixing. The mixed BNNS/GO dispersion was then sealed in a 100 mL Teflon-lined autoclave and placed in an oven for 12 h at 180 °C to reduce GO and induce self-assembly. After that, the BG hydrogel was obtained and further freeze-dried to fabricate BG aerogel. In order to explore the self-assembly modes of high-content BNNSs, small amounts of GO nanosheets were used as cross-linking agents as much as possible. Thus, the hybrid BG aerogels with different BNNS contents of 80, 85, 90, and 95 wt% were prepared to verify the stability and efficiency of the support frameworks, and named BG-80, BG-85, BG-90, and BG-95, respectively.

2.2.3 Preparation of BNNS/rGO/PEG (BGP) composite PCMs. The composite PCM was prepared by using vacuum-assisted impregnation method. The mechanism is that under the vacuum environment, the gas inside the aerogel is pumped out to form a low-pressure area, which helps the molten PEG to automatically penetrate into the interior of the aerogel and fill its pores and voids, so that it can be fully impregnated. The specific steps are as follows. First, the raw PEG powders were heated at 90 °C for 30 min to obtain fully melted, followed by degassing 20 min to remove the air bubbles under the vacuum environment. Then the as-prepared BG aerogels were immersed into the melted PEG, and then degassed for 1 h to ensure complete impregnation of the aerogels with the PEG melt. The obtained PCMs were marked as BGP-80, BGP-85, BGP-90, and BGP-95.

2.3 Characterization

The morphology and size of BNNS and GO were characterized by transmission electron microscope (TEM, JEM-2100F, Japan) and atomic force microscope (AFM, Bruker Dimension Icon, USA). The morphology and structure of BG aerogels and BGP composites were observed by scanning electron microscope (SEM, 5 kV, Hitachi SU8010, Japan). Fourier transform infrared spectroscopy (FTIR, Bruker Vertex 70, Germany) was used to test the degree of functionalization of the BNNSs. Ultraviolet-visible (UV-vis) spectra were acquired with a spectrophotometer (3600-Plus, Japan). The chemical compositions of BG aerogel were analyzed using X-ray photoelectron spectroscopy (XPS, Thermo Fisher Scientific K-Alpha, USA).

All PCM samples were polished with fine sandpaper before testing. X-ray diffraction (XRD, Bruker D8 Advance, Germany) patterns were recorded at a scanning speed of 5° min^{-1} over the diffraction angles of 10–60° (2θ). Thermogravimetric analysis (TGA, 550, USA) was performed with temperature increasing at 10 °C min^{-1} from 30 to 800 °C in nitrogen atmosphere. Differential scanning calorimetry (DSC, Q2000, USA) was conducted at the heating and cooling rate of 10 °C min^{-1} in the range of 0–100 °C under nitrogen atmosphere to examine the phase change behavior. A series of infrared images were taken to record the thermal response of the composite PCMs by an infrared thermal imager (TA-60, Shenzhen Dianyang Technology Co., Ltd). The thermal diffusivities of the composite PCMs were determined by laser flash apparatus (LFA 467, Netzsch, Germany) after spraying both surfaces with a thin layer of graphite. The thermal conductivities (κ) were calculated by the equation: $\kappa = \alpha \times \rho \times C_p$, where α, C_p and ρ are the thermal diffusivity, specific heat capacity, and the density of the sample, respectively.

3. Results and discussion

Fig. 1a illustrates the preparation of BG aerogels and BGP composite PCMs. Firstly, the two-dimensional (2D) BNNSs were obtained by ball milling method. A certain amount of IPA solution was introduced for both dispersion and exfoliation.[24] The rigid and thick bulk h-BN powders were transformed into flexible and thin BNNSs with a lateral size of about 800 nm and few layers (Fig. S1† and 1b). The GO nanosheets with a lateral size of 5–8 μm were used as initiators to assemble BNNSs (Fig. S2†). BNNSs and GO dispersions were uniformly mixed, and then self-assembled into BG hydrogels during hydrothermal process. After freeze-drying, the BG aerogels were

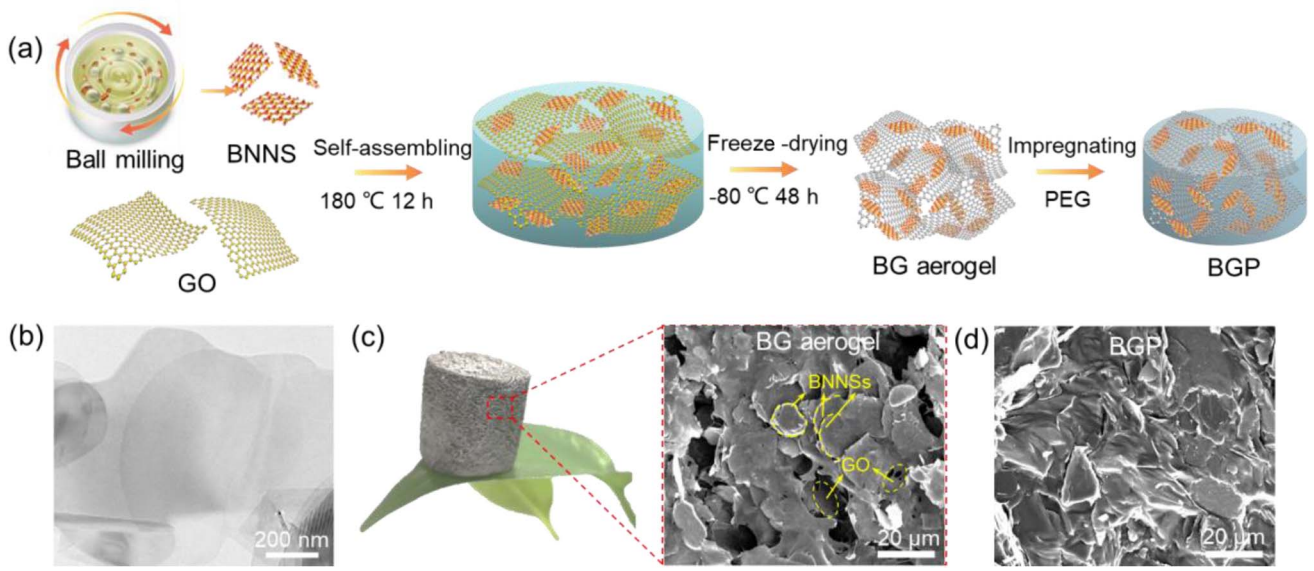

Fig. 1 (a) Scheme illustrating the preparation of BGP; (b) TEM image of BNNS; (c) digital picture of lightweight BG aerogel (95 wt% for BNNS) and the corresponding SEM image; (d) SEM image of BGP composite.

obtained even at high BNNSs content of 95 wt%. As shown in Fig. 1c, the BG-95 aerogel is lightweight that can stand freely on a green leaf due to its high porosity and low density. The typical morphology and structure of the BG-95 aerogel was characterized by SEM, the BNNSs are overlapped to form 3D continuous networks, both the surface and interlayers of which are covered by a thin layer of rGO nanosheets that acts as bridges (yellow labels in Fig. 1c). Finally, the fully filled BGP-95 composite PCMs can be prepared by vacuum-assisted impregnation method (Fig. 1d).

Fig. 2 compares the morphologies and structures of the BG-80, 85, 90 and 95 aerogels. As can be seen from the macroscopic pictures, the macro volume size of the BG aerogels gradually grows as the mass of BNNSs increases. From the microscopic SEM image of BG-80 aerogel in Fig. 2a, BNNSs are dispersed and tightly wrapped in the rGO network skeleton with macropores of ~100 μm. However, the 80 wt% BNNSs content for BG-80 aerogel does not allow for the formation of continuous sheet-to-sheet overlaps (see yellow circles in Fig. 2a), which leads to a large interfacial thermal resistance, resulting in a limited increase in thermal conductivity.[25] As the BNNS mass ratio increased to 85 wt%, BNNSs can be interconnected layer by layer and fully adhered to the skeleton, forming a continuous network structure with interlaced macro- and micro-pores (Fig. 2b). Although the porous skeletal structure remains for BG-90 aerogel, the partly stacked and collapsed BNNSs are found (seen in yellow circles of Fig. 2c). In addition, only microporous structures and totally collapsed macropores are observed in Fig. 2d for BG-95 aerogel due to the small amount of only 5 wt% GO in it. Nevertheless, BNNSs can still be bridged by

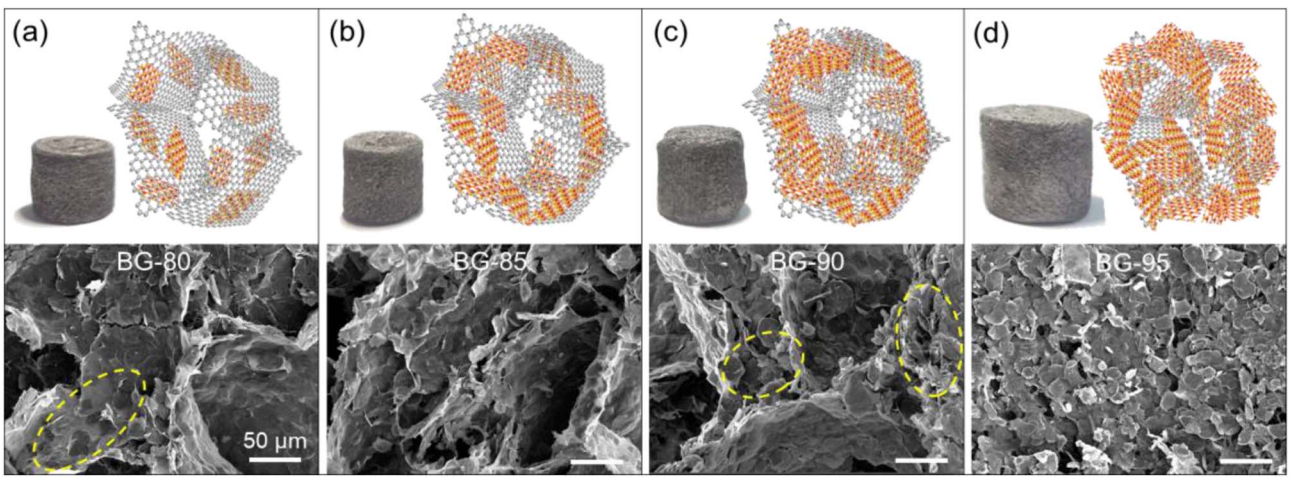

Fig. 2 Macroscopic picture, schematic diagram, and SEM image of (a) BG-80, (b) BG-85, (c) BG-90, and (d) BG-95 aerogel.

rGO nanosheets and form a stable 3D porous aerogel. Thus, a suitable BNNS content contributes to forming continuous thermal conductivity pathways and stable skeleton structure.

FTIR spectrum in Fig. 3a shows a new vibration peak of –OH at 3421 cm^{-1} and two obvious characteristic peaks located at 821 cm^{-1} (out-of-plane B–N–B bending vibration) and 1371 cm^{-1} (in-plane B–N stretching vibration) of BNNSs.[26] Such result indicates that –OH functional groups are introduced onto BNNSs during IPA-assisted ball milling process. To investigate the interactions existing between BNNSs and GO nanosheets, we have characterized the UV-vis absorbance of all BG aerogels in aqueous dispersions (Fig. 3b) and the XPS of typical BG-85 aerogel (Fig. 3c–f). As previously reported, the GO nanosheets have an absorption peak centered at 228 nm, representing the π–π transition to the aromatic C–C bond.[27] As the mass of BNNSs increases from 80 to 100 wt%, the characteristic absorption peaks are blue-shifted from 215 to 209 nm, which is attributed to the electron transfer between BNNSs and GO nanosheets originated from strong π–π stacking interactions.[28,29]

From the XPS total spectrum in Fig. 3c, it can be clearly observed that the B, N, C and O elements exist in BG-85 aerogel. The deconvoluted B 1s spectra in Fig. 3d reveal a strong binding energy peak at 190.5 eV attributed to B–N bond, since a B atom is surrounded by three N atoms. While another binding energy peak at 191.3 eV is assigned to B–O bond.[30] The N 1s spectra in Fig. 3e show two binding energy peaks at 398.3 and 399.1 eV corresponding to N–B and N–H bonds, respectively.[31] These results provide evidence that no covalent bonds are formed between BNNS and GO nanosheets. Furthermore, the deconvoluted C 1s spectra (Fig. 3f) exhibits two main binding energy peaks at 284.7 and 285.8 eV referring to C–C and C–O bonds, respectively.[32] O 1s spectrum (Fig. S3†) exhibits a relative strong binding energy peak at 532.7 eV assigned to the O–B bond, and a weak binding energy peak at 531.0 eV is assigned O–C bond. XPS spectra have demonstrated that the successful reduction reactions occur during the formation of BG aerogels with only small amounts of C–O functional groups present. Moreover, there is no covalent bonds formation between BNNSs and GO nanosheets, while the main interactions between them are π–π stacking and van der Waals force.[33]

The XRD patterns were tested by selecting the cross-section of PCMs as the test surface (as illustrated in Fig. S4†). For the pure PEG, Fig. 4a presents two diffraction peaks at 19.4° and 23.3° corresponding to the (120) and (132) crystal planes, respectively, which remain in the XRD patterns of the BGP composite PCMs. Moreover, the two characteristic peaks at approximately 27.0° and 41.8° attributed to the (002) and (100) crystallographic planes of BNNSs, which are relative to the parallel and perpendicular oriented BNNSs, respectively.[34,35] The calculated (I_{002}/I_{100}) intensity ratios of the BGP composites are various from 2.7 to 8.3. The lower intensity ratios indicate that the BNNSs are arranged with a random orientation, owing to the near-isotropic 3D thermally conductive networks.[36] Further verified by the through-plane/in-plane thermal conductivities of the samples in Fig. 4b, the BGP composite PCMs show simultaneous increases both in through-plane and in-plane thermal conductivities. Especially the BGP-85 has near-

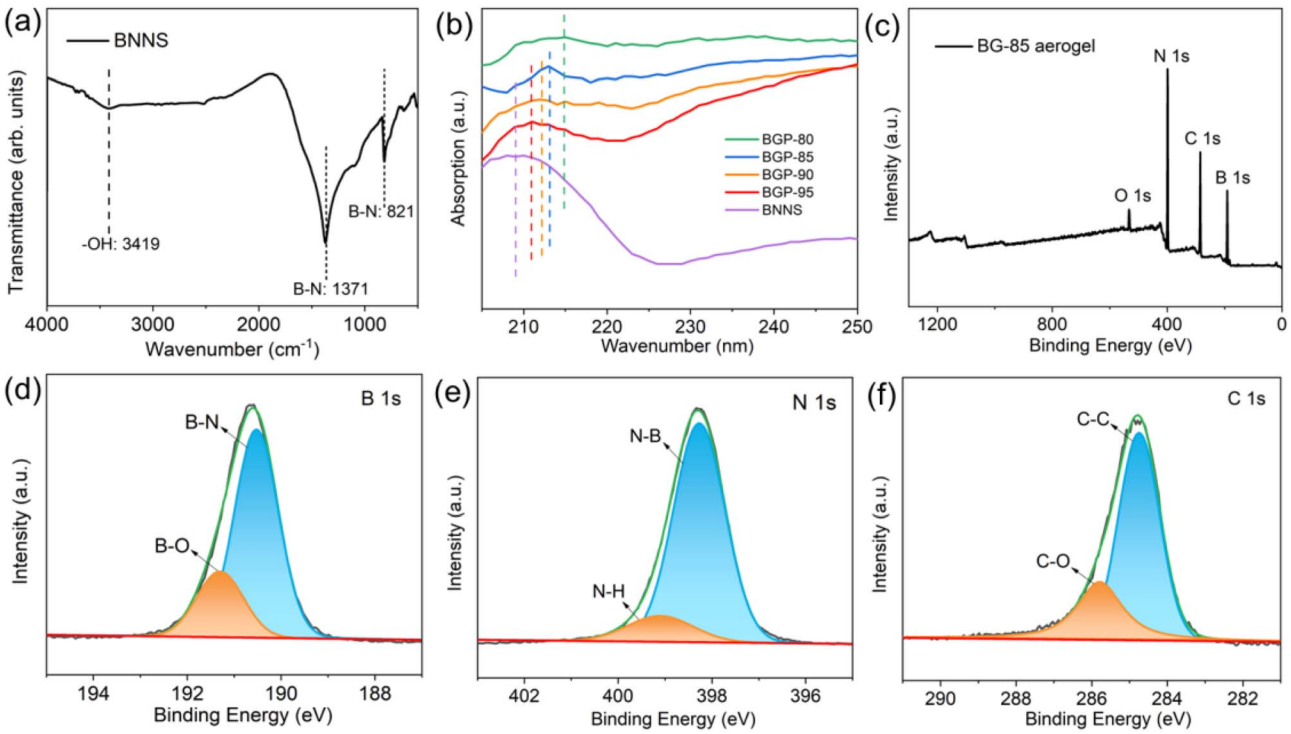

Fig. 3 (a) FTIR of BNNSs; (b) UV-vis spectra of BG aerogels (with 80, 85, 90, and 95 wt% BNNS) and BNNS; (c) XPS total spectrum of the BG-85 aerogel; (d–f) high-resolution deconvoluted XPS spectra of B 1s, N 1s and C 1s of BG-85 aerogel.

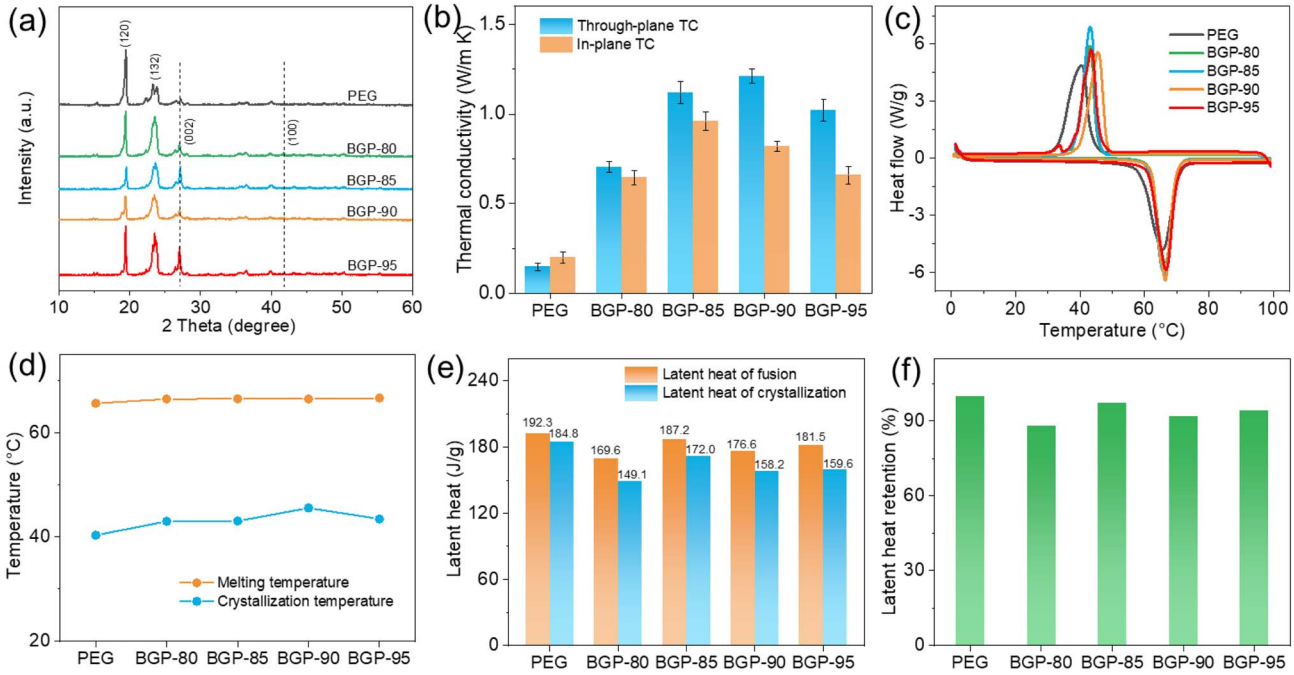

Fig. 4 Properties of the PEG and BGP composite PCMs. (a) XRD patterns; (b) through-plane/in-plane thermal conductivities; (c) DSC curves at 10 °C min^{-1}; (d) melting temperatures and crystallization temperatures; (e) specific parameters of latent heat; (f) latent heat retention.

isotropic thermal conductivity with a through-plane thermal conductivity of 1.12 W m^{-1} K^{-1} and an in-plane thermal conductivity of 0.96 W m^{-1} K^{-1}, which are almost 5 times higher than those of pure PEG. As the BNNS content increases to 90 wt%, the through-plane thermal conductivity goes up to 1.21 W m^{-1} K^{-1}. The in-plane thermal conductivity of BGP-90 is reduced to 0.82 W m^{-1} K^{-1}, which is the result of nanosheets stacking due to partial collapse caused by excessive filling of BNNSs (Fig. 2c). The accumulation of BNNSs weakens its intrinsic thermal conductivity, resulting in a further reduction in the thermal conductivity of BGP-95. Moreover, the through-plane thermal conductivity (1.02 W m^{-1} K^{-1}) for the BGP-95 is much higher than its in-plane thermal conductivity (0.66 W m^{-1} K^{-1}) due to the collapsed macropore structure of BG-95 aerogel (Fig. 2d).

DSC tests were carried out to determine the latent heat of the composite PCMs. As shown in Fig. 4c, both PEG and BGP composite PCMs exhibit obviously endothermic and exothermic peaks due to the melting and cooling. Typically, the melting and crystallization temperature ranges of pure PEG are 49.7–75.7 °C and 47.5–27.3 °C, respectively (specific parameters in Table S1†). The binding effect of the BG skeleton in BGP composites on the PEG molecular chain slightly increases the melting and crystallization temperature and rate. Thus, the endothermic and exothermic peaks of BGP composites are sharper than those of pure PEG, where the melting and crystallization temperature ranges of BGP composite PCMs are 51.6–76.6 °C and 50.5–30.2 °C, respectively. The corresponding phase change temperatures summarized in Fig. 4d also demonstrates the slight increase in both melting and crystallization temperature. The latent heat of the composite PCMs may decrease to a certain degree, as shown in Fig. 4e. The BG content was estimated by TG results (Fig. S5†). Specifically, the BGP-85 composite PCM with 7.5 wt% BG nanosheets has a high latent heat capacities of 187.2 and 172.0 J g^{-1}, when the BGP-85 was changed from solid to liquid, and from liquid to solid. The reduction of the latent heat capacity of the composite PCMs is possibly attributed to the presence of the BG support frameworks, which reduces the PEG content and restricts the motion of PEG chains.[13,37]

The latent heat retention (λ, %) was calculated by the following equation[38] and shown in Fig. 4f.

$$\lambda = \frac{\Delta H_{m(BGP)}}{\Delta H_{m(PEG)}} \times 100\%$$

where $\Delta H_{m(BPG)}$ and $\Delta H_{m(PEG)}$ represent the latent heat of fusion of BPG composite PCMs and pure PEG, respectively.

The calculated latent heat retentions of BGP-80, 85, 90, and 95 are 88.2%, 97.3%, 91.8%, and 94.4%, respectively. Results demonstrate that the BGP-85 composite PCM possesses excellent heat storage capacity and high latent heat retention, which is due to the intricate porous structure and continuous thermal pathways formed by the BG-85 aerogel with an appropriate BNNS loading, allowing the corresponding BGP-85 to be used as a promising PCM for the needs of waste heat recovery.

The crucial challenge in the practical use of organic PCMs is to avoid the leakage of the melted PEG during phase change.[39,40] The shape-stability of pure PEG and BGP composite PCMs is directly demonstrated by a leakage test using an oven under 90 °C, as shown in Fig. 5a. The pure PEG is destroyed in shape and completely melted into flowing liquid. The BGP composite PCMs remain good shape stability and only a small amount of liquid leakage is present at the edge of the BGP-95 sample. The

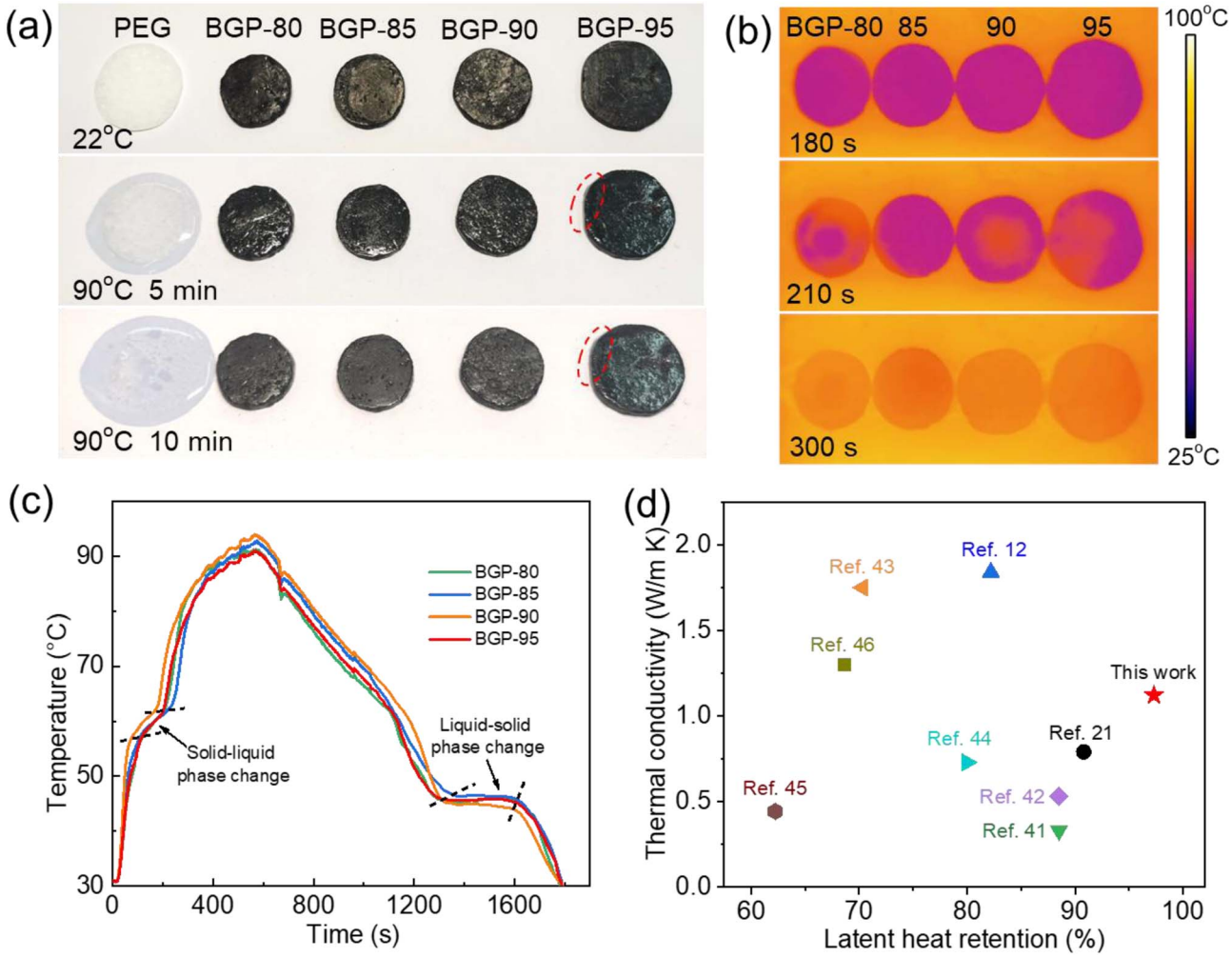

Fig. 5 (a) Digital pictures for the leaking tests of pure PEG and BGP composite PCMs; (b) recorded morphological variations by the infrared thermal imager; (c) temperature–time curves of the composite PCMs; (d) thermal conductivity–latent heat retention in h-BN systems of PCMs based on previous works.

excellent encapsulation stability of the BGP-80, 85, and 90 composite PCMs is attributed to the multi-network structure that is interwoven with macro- and micro-pores. This also indicates that 3D frameworks prepared by BNNS aerogels with small amount of GO sheets show favorable interaction with PEG and significantly improve the shape stability of the composite PCMs.

To evaluate whether the composite PCMs have enough ability for thermal storage and fast heat transfer, their thermal responses were measured directly with an infrared thermal imager. The four composite PCMs (BGP-80, 85, 90 and 95) were heated on hot plate with a constant temperature (90 °C) to accelerate the simulated sunlight conditions. Meanwhile, the temperature evolution with time at the center position of the composite PCMs were recorded precisely. The infrared images in Fig. 5b show that the surface temperature of the composite PCMs is almost uniform during the solid–liquid phase change process when being heated for 180 s. After all PEG crystallites are completely melted, the surface temperature of the composite PCMs is further enhanced with the heating time increases. From the infrared images at 210 s, the color of the composite PCMs changed at different positions and to different degrees. After being heated for 300 s, the surface temperature of the composite PCMs increases up to 90 °C, which still hold the shape well without leaking liquid (Fig. 5a). Specifically analyzed through the temperature–time curves in Fig. 5c, the BGP-90 composite has a faster heating rate due to its high through-plane thermal conductivity. And when the surface temperature of all the composite PCMs quickly increases to above 55 °C, a phase change has already occurred at this temperature.[13] Further increasing the heating time leads to a slight enhancement of the surface temperature for a long time and a plateau is present in the temperature evolution curve, representing the solid–liquid phase change process. That is, the heat energy is stored through the melting of PEG crystallites. It is worth noting that the BGP-85 composite shows a broader plateau, indicating that it has the best thermal storage ability that can absorb more heat for long time due to its intricate 3D network structure. After being irradiated for 10 min, the hot plate was switched off and the composite PCMs were naturally cooled down to room

temperature. Similarly, a plateau representing the liquid–solid phase change process is observed in the cooling curves. The surface temperature is maintained at a relatively high level (about 44–47 °C) for a long time, and the stored heat energy is released through the crystallization of PEG crystallites.

With regard to the assembly of 3D support frameworks for PCMs, our near-isotropic BNNS aerogel designed with interlaced macro-/micro-pores exhibits good thermal conductivity, high latent heat retention and excellent encapsulation ability. We compared the thermal conductivity and latent heat retention with previous works in the area of PCMs using h-BNs/BNNSs as fillers.[13,41–47] As shown in Fig. 5d, although the thermal conductivity is slightly less than that in some reports, the superior latent heat of fusion retention, which benefit from the impressive 3D interconnected network assembled with small amounts of fillers that can support enough PEG matrix. Thus, our prepared composite PCMs provide highly efficient thermal energy storage.

4. Conclusions

In summary, with the aid of small amount of GO nanosheets, the BNNSs have been successfully self-assembled into BG aerogels by hydrothermal and freeze-drying processes. The constructed BG aerogels with interlaced macro-/micro-pores are ideal for use as support frameworks to encapsulate PEG, and the corresponding BGP composite PCMs exhibit enhanced thermal conductivity, high latent heat retention, and good encapsulation ability. Especially for BGP-85 composite PCM, which has been proved to have superior integrated performance. The BGP-85 composite PCM shows high thermal conductivity of 1.12 W m^{-1} K^{-1}, high latent heat (187.2 J g^{-1}) with a retention of 97.3% of the pure PEG, and excellent shape ability without any leakage even under 90 °C for 10 min. With its structural advantages and outstanding performances, the composite PCM can be further used in applications such as energy storage systems and thermal management of electronic devices.

Conflicts of interest

There are no conflicts to declare.

Acknowledgements

This research was supported by the Zhuhai Basic and Applied Basic Research Project (No. 2220004002790), the China Postdoctoral Science Foundation (CPSF, No. 2023M734088), the National Natural Science Foundation of China (NSFC, No. 12005318), and the Science and Technology on Reactor System Design Technology Laboratory (HT-KFKT-02-2019017).

References

1 H. Zhu, Y. Li, Z. Fang, J. Xu, F. Cao, J. Wan, C. Preston, B. Yang and L. Hu, *ACS Nano*, 2014, **8**, 3606–3613.
2 W. Luo, Y. Wang, E. Hitz, Y. Lin, B. Yang and L. Hu, *Adv. Funct. Mater.*, 2017, **27**, 1701450.
3 Y. Zhan, Z. Long, X. Wan, C. Zhan, J. Zhang and Y. He, *Ceram. Int.*, 2017, **43**, 12109–12119.
4 D. Pan, F. Su, H. Liu, Y. Ma, R. Das, Q. Hu, C. Liu and Z. Guo, *Chem. Rec.*, 2020, **20**, 1314–1337.
5 X. Wang and P. Wu, *Chem. Eng. J.*, 2018, **348**, 723–731.
6 M. Li, M. Wang, X. Hou, Z. Zhan, H. Wang, H. Fu, C.-T. Lin, L. Fu, N. Jiang and J. Yu, *Composites, Part B*, 2020, **184**, 107746.
7 K. Uosaki, G. Elumalai, H. Noguchi, T. Masuda, A. Lyalin, A. Nakayama and T. Taketsugu, *J. Am. Chem. Soc.*, 2014, **136**, 6542–6545.
8 Z. Liu, Y. Gong, W. Zhou, L. Ma, J. Yu, J. C. Idrobo, J. Jung, A. H. MacDonald, R. Vajtai and J. Lou, *Nat. Commun.*, 2013, **4**, 1–8.
9 W. Lei, V. N. Mochalin, D. Liu, S. Qin, Y. Gogotsi and Y. Chen, *Nat. Commun.*, 2015, **6**, 1–8.
10 W. Wu, H. Liu, Z. Wang, P. Lv, E. Hu, J. Zheng, K. Yu and W. Wei, *Ceram. Int.*, 2021, **47**, 33926–33929.
11 L. Wan, C. Liu, D. Cao, X. Sun and H. Zhu, *ACS Appl. Polym. Mater.*, 2020, **2**, 3001–3009.
12 D. Pan, J. Dong, G. Yang, F. Su, B. Chang, C. Liu, Y.-C. Zhu and Z. Guo, *Adv. Compos. Hybrid Mater.*, 2022, **5**, 58–70.
13 F. Xue, X.-z. Jin, X. Xie, X.-d. Qi, J.-h. Yang and Y. Wang, *Nanoscale*, 2019, **11**, 18691–18701.
14 M. Liu, S.-W. Chiang, X. Chu, J. Li, L. Gan, Y. He, B. Li, F. Kang and H. Du, *Ceram. Int.*, 2020, **46**, 20810–20818.
15 G. Li, M. Zhu, W. Gong, R. Du, A. Eychmüller, T. Li, W. Lv and X. Zhang, *Adv. Funct. Mater.*, 2019, **29**, 1900188.
16 Z. Qian, H. Shen, X. Fang, L. Fan, N. Zhao and J. Xu, *Energy Build.*, 2018, **158**, 1184–1188.
17 S. Karaman, A. Karaipekli, A. Sarı and A. Bicer, *Sol. Energy Mater. Sol. Cells*, 2011, **95**, 1647–1653.
18 M. Xin, M. Fang, Z. Huang, Y. Liu, Y. Huang, R. Wen, T. Qian and X. Wu, *Sci. Rep.*, 2015, **5**, 12964.
19 C. Lei, K. Wu, L. Wu, W. Liu, R. Du, F. Chen and Q. Fu, *J. Mater. Chem. A*, 2019, **7**, 19364–19373.
20 J. Chen, X. Huang, Y. Zhu and P. Jiang, *Adv. Funct. Mater.*, 2017, **27**, 1604754.
21 J. Yang, X. Li, S. Han, Y. Zhang, P. Min, N. Koratkar and Z.-Z. Yu, *J. Mater. Chem. A*, 2016, **4**, 18067–18074.
22 J. Chen, Y. Zhang, M. Zhang, B. Yao, Y. Li, L. Huang, C. Li and G. Shi, *Chem. Sci.*, 2016, **7**, 1874–1881.
23 M. H. Wahid, X. Chen, C. T. Gibson and C. L. Raston, *Chem. Commun.*, 2015, **51**, 11709–11712.
24 W. L. Song, P. Wang, L. Cao, A. Anderson, M. J. Meziani, A. J. Farr and Y. P. Sun, *Angew. Chem.*, 2012, **124**, 6604–6607.
25 V. Guerra, C. Wan and T. McNally, *Prog. Mater. Sci.*, 2019, **100**, 170–186.
26 D. Pan, X. Zhang, G. Yang, Y. Shang, F. Su, Q. Hu, R. R. Patil, H. Liu, C. Liu and Z. Guo, *Ind. Eng. Chem. Res.*, 2020, **59**, 20371–20381.
27 C. Zhang, L. Ren, X. Wang and T. Liu, *J. Phys. Chem. C*, 2010, **114**, 11435–11440.

28 M. Wang, T. Zhang, D. Mao, Y. Yao, X. Zeng, L. Ren, Q. Cai, S. Mateti, L. H. Li and X. Zeng, *ACS Nano*, 2019, **13**, 7402–7409.
29 Z. Gao, C. Zhi, Y. Bando, D. Golberg and T. Serizawa, *ACS Appl. Mater. Interfaces*, 2011, **3**, 627–632.
30 K. Kim, M. Kim, Y. Hwang and J. Kim, *Ceram. Int.*, 2014, **40**, 2047–2056.
31 J. Qu, Q. Li, C. Luo, J. Cheng and X. Hou, *Coatings*, 2018, **8**, 214.
32 V. Yadav, N. Niluroutu, S. D. Bhat and V. Kulshrestha, *ACS Appl. Energy Mater.*, 2020, **3**, 7091–7102.
33 D. Lee, S. H. Song, J. Hwang, S. H. Jin, K. H. Park, B. H. Kim, S. H. Hong and S. Jeon, *Small*, 2013, **9**, 2602–2610.
34 C. Yuan, B. Duan, L. Li, B. Xie, M. Huang and X. Luo, *ACS Appl. Mater. Interfaces*, 2015, **7**, 13000–13006.
35 H. Shen, J. Guo, H. Wang, N. Zhao and J. Xu, *ACS Appl. Mater. Interfaces*, 2015, **7**, 5701–5708.
36 L. Xu, K. Zhan, S. Ding, J. Zhu, M. Liu, W. Fan, P. Duan, K. Luo, B. Ding, B. Liu, Y. Liu, H. M. Cheng and L. Qiu, *ACS Nano*, 2023, **17**, 4886–4895.
37 G.-Q. Qi, C.-L. Liang, R.-Y. Bao, Z.-Y. Liu, W. Yang, B.-H. Xie and M.-B. Yang, *Sol. Energy Mater. Sol. Cells*, 2014, **123**, 171–177.
38 X. Li, X. Sheng, Y. Guo, X. Lu and J. Gu, *J. Mater. Sci. Technol.*, 2021, **86**, 171–179.
39 W. Aftab, X. Huang, W. Wu, Z. Liang, A. Mahmood and R. Zou, *Energy Environ. Sci.*, 2018, **11**, 1392–1424.
40 W. Aftab, A. Usman, J. Shi, K. Yuan, M. Qin and R. Zou, *Energy Environ. Sci.*, 2021, **14**, 4268–4291.
41 J. Yang, L.-S. Tang, R.-Y. Bao, L. Bai, Z.-Y. Liu, W. Yang, B.-H. Xie and M.-B. Yang, *J. Mater. Chem. A*, 2016, **4**, 18841–18851.
42 J. Wang, H. Xie, Z. Xin, Y. Li and L. Chen, *Sol. Energy*, 2010, **84**, 339–344.
43 X. Fang, L.-W. Fan, Q. Ding, X.-L. Yao, Y.-Y. Wu, J.-F. Hou, X. Wang, Z.-T. Yu, G.-H. Cheng and Y.-C. Hu, *Energy Convers. Manage.*, 2014, **80**, 103–109.
44 J. Yang, G.-Q. Qi, L.-S. Tang, R.-Y. Bao, L. Bai, Z.-Y. Liu, W. Yang, B.-H. Xie and M.-B. Yang, *J. Mater. Chem. A*, 2016, **4**, 9625–9634.
45 S.-G. Jeong, J.-H. Lee, J. Seo and S. Kim, *Int. J. Heat Mass Transfer*, 2014, **71**, 245–250.
46 N. Sun and Z. Xiao, *Energy Fuels*, 2017, **31**, 10186–10195.
47 J. Yang, L.-S. Tang, R.-Y. Bao, L. Bai, Z.-Y. Liu, W. Yang, B.-H. Xie and M.-B. Yang, *Chem. Eng. J.*, 2017, **315**, 481–490.